

**Fusion-fission studies in the  $^{20}\text{Ne}+^{181}\text{Ta}$  reaction at  $E/A = 7.5$  and  $9$  MeV/nucleon**

R. Tripathi, K. Sudarshan, A. Goswami,\* R. Guin, and A. V. R. Reddy  
*Radiochemistry Division, Bhabha Atomic Research Centre, Mumbai-400085, India*  
 (Received 28 March 2006; published 27 July 2006)

Mass and mass resolved angular distribution of the fission products have been measured in the  $^{20}\text{Ne}+^{181}\text{Ta}$  reaction at  $E_{\text{lab}} = 150$  and  $180$  MeV using recoil catcher technique followed by off-line  $\gamma$ -ray spectrometry. Recoil range distribution (RRD) of the evaporation residues (ERs) have been measured at  $E_{\text{lab}} = 180$  MeV. Due to high angular momentum of the fissioning nucleus, variances of the mass distribution in the present system have been found to be higher than those in similar systems involving comparatively less angular momentum. Significant contribution from noncompound nucleus processes such as deep inelastic collisions (DIC) and incomplete fusion reaction (ICF) is expected in the present system due to high angular momentum. The code HICOL predicts that the noncompound nucleus process would result in fission like events. In the present study, experimental fission cross sections are in reasonably good agreement with the calculation of statistical model code PACE2. Measurement of the ER cross section indicates significant contribution from the ICF reaction. The recoil range distributions of the ERs could resolve the complete fusion (CF) and ICF channels and were used to obtain ICF cross section. The experimentally measured ICF cross section accounts for almost entire cross section between  $l_{\text{crit}}$  and  $l_{\text{max}}$ , indicating ICF reaction to be the dominant non-compound nucleus process at beam energies of the present study. DIC products could not be detected at both the beam energies. At these beam energies, the entrance channel pocket configuration for many collision trajectories is expected to be more elongated compared to the unconditional saddle point and, therefore, significant contribution from noncompound nucleus fission (i.e., fission without passing through the unconditional saddle point) is expected. However, the experimental anisotropies of fission products could be reproduced by the statistical theory calculation after considering the change in the saddle point shape with angular momentum of the fissioning nucleus. No correlation between the angular anisotropy and mass asymmetry of the fission products was observed in the present study.

DOI: [10.1103/PhysRevC.74.014610](https://doi.org/10.1103/PhysRevC.74.014610)

PACS number(s): 25.70.Jj

**I. INTRODUCTION**

The process of nuclear fusion is defined as the capture of a projectile by the target nucleus forming fully equilibrated compound nucleus. The compound nucleus subsequently decays by emission of particles and  $\gamma$ -rays to form evaporation residues. The compound nucleus may also undergo fission if excitation energy is higher than the fission barrier. Depending upon the beam energy and entrance channel mass asymmetry, there are several possibilities other than the formation of a fully equilibrated compound nucleus in the collision of an energetic heavy ion with a target nucleus. The collision trajectories with  $l < l_{\text{crit}}$  are trapped in the pocket in the entrance channel potential [1] leading to fusion. On the other hand, for the collision trajectories with  $l > l_{\text{crit}}$ , pocket in the entrance channel potential vanishes, and therefore such trajectories will lead to noncompound nucleus processes such as deep inelastic collisions (DIC) and incomplete fusion reaction (ICF). DIC is characterized by substantial dissipation of initial kinetic energy and angular momentum. The time-scale of deep inelastic collisions is shorter than the compound nucleus life-time, but long enough for the exchange of significant number of nucleons between the target and the projectile. The DIC product masses are close to the mass of the projectile and target [2]. The kinetic energy spectra of the products formed in deep inelastic collisions extend up to the exit channel Coulomb

barrier starting from the beam energy [2,3]. In the reactions with lighter projectiles, incomplete fusion reaction involving partial capture of the projectile by the target nucleus is observed [4–6]. Incomplete fusion reactions are characterized by the forward peaked angular distribution of projectile like fragments (PLFs) which are predominantly emitted at the beam velocity. The linear momentum transfer in the ICF reactions is less than that in complete fusion (CF) resulting in lower range of the evaporation residues formed in the ICF reaction [7]. In the CF reaction, the composite system relaxes in all degrees of freedom to form a fully equilibrated compound nucleus. However, for the sufficiently heavy systems, composite nucleus may undergo fission without forming the fully equilibrated compound nucleus [8–10]. Contribution from noncompound nucleus fission results in deviation of the fission fragment angular anisotropy from statistical theory calculation [10,11] and suppression in the formation of evaporation residues [12,13].

The reaction mechanism in collision between the two nuclei mainly depends on the entrance channel parameters, namely, beam energy and mass asymmetry. For systems with large Coulomb repulsion in the entrance channel (symmetric systems), DIC has been reported as the major noncompound nucleus channel [2,14]. For systems with higher entrance channel mass asymmetry, ICF has been reported to be the dominant noncompound nucleus channel [4]. In such systems, DIC has been observed at higher beam energies [15]. Mathews *et al.* have attributed the mass transport from the target to the projectile in  $^{20}\text{Ne}$ -induced reactions on  $^{\text{nat}}\text{Cu}$

\*Corresponding author, Email: [agoswami@barc.gov.in](mailto:agoswami@barc.gov.in)

and  $^{197}\text{Au}$  at beam energies of 172 and 252 MeV to DIC [16]. At intermediate bombarding energies, noncompound nucleus fission is another process other than DIC and ICF. Measurement of the fission fragment angular distribution in  $^{19}\text{F}+^{197}\text{Au}$  reaction by Ikezoe *et al.* [17] has shown contribution from noncompound nucleus fission at  $E_{\text{lab}} = 160$  MeV. These studies show that several reaction channels open up at medium bombarding energies ( $E/A \sim 8$  MeV/nucleon). In spite of extensive work carried out in this area, a complete understanding of the mechanism of various types of reactions and their dependence on beam energy and entrance channel mass asymmetry is still lacking. Measurement of fission products and evaporation residues in a nuclear reaction can provide a comprehensive picture of the processes subsequent to the collision between the projectile and the target nuclei.

In order to investigate various reaction channels in  $^{20}\text{Ne}+^{181}\text{Ta}$  reaction, fission products and evaporation residues have been measured at  $E_{\text{lab}} = 150$  and 180 MeV. Mass distributions of fission products have been measured at both the energies and fission cross sections have been deduced from the mass distribution. The variances of the mass distributions determined in the present study have been compared with the literature values to investigate the effect of the angular momentum on the fission product mass distribution. At beam energy of 180 MeV,  $l_{\text{max}} (= R/\hbar \sqrt{2\mu(E_{\text{c.m.}} - V_c)})$ ;  $R$ : sum of radii of the projectile and the target  $R_P + R_T$ ;  $R_P = 1.4A_P^{1/3}$  and  $R_T = 1.4A_T^{1/3}$ ,  $A_P$  and  $A_T$  are the mass numbers of the projectile and the target, respectively;  $\mu$ : reduced mass of the system;  $E_{\text{c.m.}}$ : center of mass energy; and  $V_c$ : entrance channel Coulomb barrier) is  $94\hbar$  which is much higher than  $l_{\text{crit}} (= 81\hbar)$  [18] and therefore, substantial cross section for noncompound nucleus processes such as DIC and ICF is expected. In order to get the information about the mechanism of formation of evaporation residues, recoil range distributions (RRD) of ERs have been measured at  $E_{\text{lab}} = 180$  MeV. Mass resolved angular distributions of the fission products have been measured at both the energies. Measurement of the mass resolved angular distribution gives information about the correlation between angular anisotropy and mass asymmetry as observed in the proton and alpha induced fission [19–21]. From the measured angular distribution, average anisotropies at both the energies have been deduced and compared with the statistical theory calculations to investigate the contribution from noncompound nucleus fission.

## II. EXPERIMENTAL

Experiments were carried out at Variable Energy Cyclotron Centre, Kolkata, India. For the mass distribution studies, target assembly consisting of a self-supporting tantalum target ( $1.8$  mg/cm<sup>2</sup>), a thin aluminium catcher foil ( $2.25$  mg/cm<sup>2</sup>) and another thick aluminium catcher foil ( $6.75$  mg/cm<sup>2</sup>) was bombarded with 180 MeV  $^{20}\text{Ne}$  beam. Thin catcher foil was kept to stop the evaporation residues recoiling out of the target and thick catcher foil was kept to completely stop the fission products escaping from the target and the thin catcher foil. As residues were completely stopped in the thin catcher foil, they could be unambiguously distinguished from the fission

products. At  $E_{\text{lab}} = 150$  MeV, single catcher foil of thickness  $6.75$  mg/cm<sup>2</sup> was used. At each beam energy, irradiation was carried out for about six hours. After irradiation, target and catcher foils were separately assayed for the  $\gamma$ -ray activity of the fission products and evaporation residues.

For the measurement of recoil range distributions (RRDs), thin target of tantalum oxide was prepared by vacuum evaporation of tantalum oxide on aluminium backing of thickness  $500$   $\mu\text{g}/\text{cm}^2$ . Thickness of tantalum oxide layer was  $200$   $\mu\text{g}/\text{cm}^2$ . Target was bombarded with 180 MeV  $^{20}\text{Ne}$  beam for about 8 h with aluminium backing facing the beam. A stack of aluminium catcher foils (thickness  $203$   $\mu\text{g}/\text{cm}^2$ ) was used to stop the evaporation residues.

For angular distribution studies, self-supporting target of  $^{181}\text{Ta}$  of thickness  $1.8$  mg/cm<sup>2</sup> was placed at  $45^\circ$  with respect to the beam direction. A cylindrical irradiation chamber of length 130 mm and inner diameter of 155 mm was used. Aluminium catcher foil of thickness  $6.75$  mg/cm<sup>2</sup> was mounted on the inner wall of the cylinder covering an azimuthal angle of  $180^\circ$  and  $\theta_{\text{lab}}$  from  $90^\circ$  to  $30^\circ$ . In the forward direction catcher foil was placed on the inner flat surface of the front cover of the chamber, covering  $\theta_{\text{lab}}$  from  $30^\circ$  to  $0.3^\circ$ . At each beam energy, irradiation was carried out for about 30 h. After the irradiation, the catcher foils were removed and cut into ten strips and each strip on an average was having an angular width of about  $9^\circ$ . The strips of the catcher foils corresponding to different laboratory angles were folded to the same geometry and assayed for the gamma ray activity of the fission products.

The  $\gamma$ -ray activity of the fission products and ERs was assayed using an HPGe detector coupled to a multichannel analyzer. The activities of the fission products and ERs were corrected for the decay after irradiation. The end of irradiation activities were used for the determination of the formation cross sections of the fission products and ERs using the standard activation equation [22]. The nuclear data of the radionuclides studied in the present work are given in Table I [23,24]. In the present work, formation cross sections of about 25 fission products were determined. In the case of feeding from the parent during the measurement of the gamma-ray activity of a fission product, decay-growth equations were solved to obtain the formation cross sections of the parent and the daughter. In the case of a radionuclide having an isomeric state, predominantly undergoing  $\beta^-/\beta^+/\text{EC}$  decay, experimentally measured yield was corrected assuming the yield of the high spin isomer to be 80% of the total yield. The formation cross sections are given in Table II. The independent and cumulative cross sections are marked by I and C, respectively, in the table.

## III. RESULTS AND DISCUSSION

### A. Mass distribution

In order to obtain the mass distribution of the fission products, the experimentally measured formation cross sections are to be corrected for the charge distribution. The procedure used for the charge distribution correction is as follows. For a given mass chain  $A$ , the mass yield  $Y(A)$  is obtained from the experimentally measured cumulative  $[CU(A, Z)]$  or

TABLE I. Relevant nuclear data of the radionuclides studied in the present work [23,24].

Nuclide	$E_\gamma$ (keV)	Gamma-ray abundance ( $I_\gamma$ )	$T_{1/2}$
$^{67}\text{Cu}$	184.6	48.7	2.58 d
$^{69}\text{Zn}^m$	438.6	94.8	13.7 h
$^{72}\text{Ga}$	834.8	95.6	14.1 h
$^{73}\text{Ga}$	297.3	80.0	4.87 h
$^{74}\text{As}$	595.8	60.3	17.78 d
$^{76}\text{As}$	559.1	44.7	26.32 h
$^{81}\text{Rb}^g$	190.4	64.3	4.58 h
$^{82}\text{Br}^g$	554.3	70.6	35.3 h
$^{82}\text{Rb}^m$	776.5	84.5	6.47 h
$^{83}\text{Rb}$	520.4	46.1	86.2 d
$^{84}\text{Rb}^g$	881.6	67.8	32.87 d
$^{86}\text{Rb}^g$	1076.6	8.78	18.66 d
$^{86}\text{Y}^m$	208.2	93.7	48.0 m
$^{87}\text{Y}^m$	381.1	78.1	12.9 h
$^{88}\text{Y}$	898.0	94.0	106.6 d
$^{89}\text{Zr}^g$	909.2	99.0	3.27 d
$^{90}\text{Y}^m$	202.5	96.5	3.19 h
$^{90}\text{Nb}^g$	141.2	69.0	14.60 h
$^{91}\text{Sr}$	555.6	61.3	9.52 h
$^{91}\text{Y}^m$	555.6	94.9	49.71 m
$^{92}\text{Sr}$	1383.9	90	2.71 h
$^{92}\text{Y}$	934.5	13.9	3.54 h
$^{93}\text{Y}$	266.9	6.99	10.1 h
$^{94}\text{Y}$	918.8	73.3	18.6 m
$^{95}\text{Zr}$	756.7	55.4	64.03 d
$^{96}\text{Nb}$	778.2	96.9	23.35 h
$^{98}\text{Nb}$	722.7	70.0	51.3 m
$^{98}\text{Nb}$	787.4	93.0	51.3 m
$^{99}\text{Mo}$	140.5	90.7	2.75 d
$^{100}\text{Rh}^g$	539.6	78.4	20.8 h
$^{101}\text{Rh}^m$	306.9	86.3	4.34 d
$^{103}\text{Ru}$	497.1	89.5	39.25 d
$^{105}\text{Rh}^g$	318.9	19.2	35.36 h
$^{106}\text{Rh}^m$	451.0	24.5	2.17 h
$^{111}\text{Ag}$	342.1	6.7	7.45 d
$^{116}\text{In}^m$	1097.3	56.2	54.15 m
$^{118}\text{Sb}^m$	253.7	94.2	5.0 h
$^{123}\text{I}$	159.0	83.3	13.2 h
$^{180}\text{Os}$	902.8	99.9	22 m
$^{181}\text{Re}$	365.5	56.4	20 h
$^{182}\text{Re}^g$	169.2	11.3	64.0 h
$^{183}\text{Re}$	162.3	23.5	70.0 d
$^{184}\text{Ir}$	390.4	25.7	3.02 h
$^{185}\text{Os}$	646.1	78	93.6 d
$^{186}\text{Ir}^b$	434.8	33.8	16.64 h
$^{186}\text{Pt}$	689.2	100 <sup>a</sup>	2.0 h
$^{188}\text{Pt}$	155.0	35.9	10.2 d
$^{189}\text{Pt}$	721.4	9.3	10.89 h
$^{190}\text{Hg}$	142.6	68	20.0 m
$^{191}\text{Hg}^m$	252.6	60	50.8 m
$^{192}\text{Hg}$	274.8	50.4	4.85 h
$^{193}\text{Hg}^m$	258.0	61.4	11.8 h
$^{194}\text{Tl}^m$	636.3	98.00	32.8 m

<sup>a</sup> $\gamma$ -ray abundance is relative.TABLE II. Formation cross sections of the fission products formed in  $^{20}\text{Ne}+^{181}\text{Ta}$  reaction at  $E_{\text{lab}} = 150$  and 180 MeV.

Nuclide	Cross section (mb)		
	$E_{\text{lab}} = 150$ MeV	$E_{\text{lab}} = 180$ MeV	
$^{67}\text{Cu}$	—	$8.05 \pm 1.6$	C
$^{69}\text{Zn}^m$	$4.14 \pm 0.35$	$8.48 \pm 0.32$	C
$^{72}\text{Ga}$	$7.24 \pm 0.58$	$14.3 \pm 0.5$	I
$^{73}\text{Ga}$	$7.01 \pm 0.57$	$9.42 \pm 0.48$	C
$^{74}\text{As}$	$2.92 \pm 0.31$	$9.64 \pm 0.94$	I
$^{76}\text{As}$	$12.8 \pm 0.5$	$22.0 \pm 1.2$	I
$^{82}\text{Br}^g$	$12.0 \pm 1.0$	$19.0 \pm 0.2$	I
$^{84}\text{Rb}^g$	$9.38 \pm 1.64$	$24.2 \pm 1.2$	I
$^{86}\text{Rb}^g$	$13.8 \pm 8.9$	$37.5 \pm 3.3$	I
$^{90}\text{Y}^m$	$23.8 \pm 0.5$	$41.2 \pm 1.5$	I
$^{91}\text{Sr}$	$6.39 \pm 0.53$	$12.3 \pm 1.4$	C
$^{91}\text{Y}^m$	$20.8 \pm 0.6$	$38.9 \pm 1.3$	I
$^{92}\text{Y}$	$13.6 \pm 2.0$	$20.5 \pm 4.4$	I
$^{95}\text{Zr}$	$14.5 \pm 2.0$	$13.9 \pm 1.6$	C
$^{96}\text{Nb}$	$20.0 \pm 1.0$	$29.8 \pm 1.2$	I
$^{98}\text{Nb}$	$8.35 \pm 0.95$	$12.2 \pm 0.9$	C
$^{99}\text{Mo}$	$26.5 \pm 0.8$	$36.6 \pm 0.7$	C
$^{103}\text{Ru}$	$36.0 \pm 1.0$	$48.1 \pm 1.8$	C
$^{105}\text{Rh}^g$	$36.2 \pm 1.6$	$40.6 \pm 4.9$	I
$^{106}\text{Rh}^m$	$14.0 \pm 1.3$	$19.0 \pm 1.3$	I
$^{111}\text{Ag}^g$	$17.2 \pm 1.2$	$19.6 \pm 1.3$	C
$^{116}\text{In}^m$	$7.48 \pm 0.46$	$11.9 \pm 1.1$	I
$^{118}\text{Sb}^m$	$6.12 \pm 0.70$	$8.48 \pm 0.32$	I
$^{123}\text{I}$	$8.64 \pm 1.13$	$19.1 \pm 2.2$	C

independent [ $IN(A, Z)$ ] yield of a fission product with mass number  $A$  and atomic number  $Z$  using the following equations:

$$Y(A) = \frac{CU(A, Z)}{FC(A, Z)}, \quad (1)$$

$$Y(A) = \frac{IN(A, Z)}{FI(A, Z)}, \quad (2)$$

where  $FC(A, Z)$  and  $FI(A, Z)$  are the fractional cumulative and independent yields respectively, which are given by the Gaussian distributions,

$$FC(A, Z) = \frac{1}{\sqrt{2\pi\sigma_Z^2}} \int_{-\infty}^{Z+0.5} e^{-(Z-Z_p)^2/2\sigma_Z^2} dZ, \quad (3)$$

$$FI(A, Z) = \frac{1}{\sqrt{2\pi\sigma_Z^2}} \int_{Z-0.5}^{Z+0.5} e^{-(Z-Z_p)^2/2\sigma_Z^2} dZ, \quad (4)$$

where  $Z_p$  and  $\sigma_Z$  are, respectively, the most probable charge and the width parameter of the isobaric yield distribution. From the experimentally measured yield of a fission product, calculation of the total chain yield  $Y(A)$  requires the knowledge of  $Z_p$  and  $\sigma_Z$  for the isobaric mass chain. Ideally, independent yields of at least three members in an isobaric chain are required to obtain these parameters. Since, it is difficult to measure three independent yields in an isobaric chain, an alternative

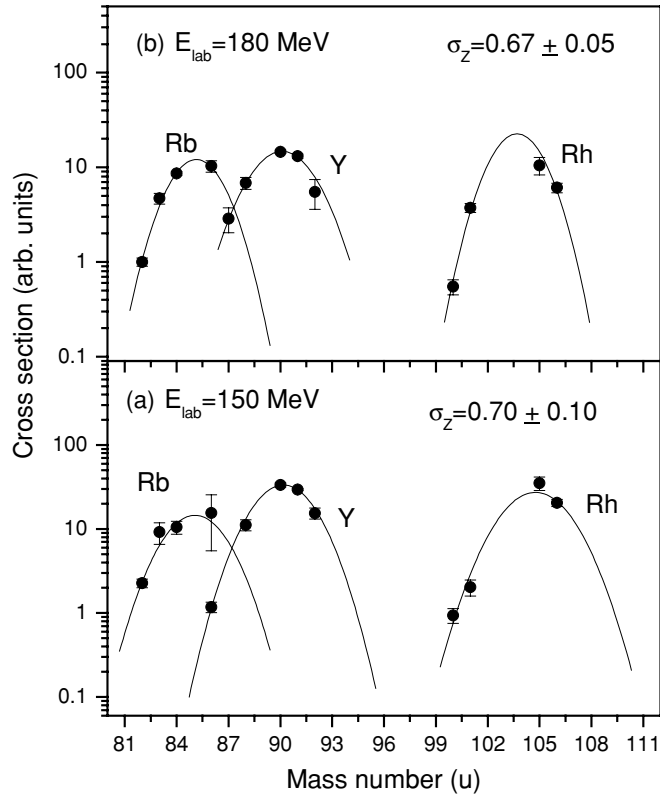


FIG. 1. Isotopic yield distributions of Rb, Y, and Rh isotopes in  $^{20}\text{Ne}+^{181}\text{Ta}$  reaction at  $E_{\text{lab}} = 150$  MeV (a) and 180 MeV (b).

approach to obtain the charge distribution parameters in fission is to determine the isotopic yield distribution of elements formed in fission. In the present study, this approach has been used to obtain charge distribution parameters using the independent yields of Rb ( $^{82,83,84,86}\text{Rb}$ ), Y ( $^{87,88,90,91,92}\text{Y}$ ), and Rh ( $^{100,101,105,106}\text{Rh}$ ) isotopes. The isotopic yield distributions of Rb, Y, and Rh isotopes at  $E_{\text{lab}} = 150$  and 180 MeV are shown in Figs. 1(a) and 1(b), respectively. Isotopic yield distributions were fitted to Gaussian function to obtain the width of the isotopic yield distribution  $\sigma_A \cdot \sigma_A$  values were converted to  $\sigma_Z$ , using the following equation [25]:

$$\sigma_Z = \frac{\sigma_A}{(A_p/Z)}, \quad (5)$$

where,  $A_p$  is the most probable mass of the isotopic yield distribution for a given  $Z$ . The average values of the  $\sigma_Z$  obtained from the isotopic yield distributions of Rb, Y, and Rh isotopes, were  $0.70 \pm 0.09$  and  $0.67 \pm 0.05$  at  $E_{\text{lab}} = 150$  and 180 MeV, respectively. The  $Z_p$  value for a mass chain with mass number  $A$  was calculated using the unchanged charge distribution (UCD) hypothesis as given by the following equation:

$$Z_p = \frac{A}{(A_{CN} - \nu_{\text{pre}})/Z_{CN}}, \quad (6)$$

where,  $A_{CN}$  and  $Z_{CN}$  are, respectively, the mass and atomic numbers of the compound nucleus.  $\nu_{\text{pre}}$  is the average number of pre-fission neutrons. An estimate of  $\nu_{\text{pre}}$  was obtained using the prescription of Kozuline *et al.* [26]. The

$Z_p$  values, calculated using the UCD hypothesis, were further corrected for the charge polarization using the prescription of Swiatecki [27]. Formation cross sections of the fission products determined using their activities in the thick catcher foil, were corrected for charge distribution to obtain the mass yields. At  $E_{\text{lab}} = 180$  MeV, fission products were partially stopped in the thin catcher foil placed before the thick one in the forward direction. The ratio of the yields of fission products in the thin catcher foil to that in the thick catcher foil was used to correct for the fission products stopped in the thin catcher foil. Since, fission products escaping in the backward direction were not detected in the present study, forward to backward ratios for the fission products were calculated using the standard kinematic equations with kinetic energy calculated using the prescription of Rossner *et al.* [28] and were used to correct for the fission products escaped in the backward direction. The mass yield distributions were fitted to the Gaussian function to obtain the fission cross section. In order to improve the fitting of the mass distribution as judged by the chi square of the fit, the  $\nu_{\text{pre}}$  values in Eq. (6) were varied. Mass distributions along with the best fits in  $^{20}\text{Ne}+^{181}\text{Ta}$  reaction at  $E_{\text{lab}} = 150$  and 180 MeV are shown in Figs. 2(a) and 2(b), respectively. The variances of mass distributions in the present system have been compared with the values reported in the literature for similar systems. The experimental values of the present measurement compare well with the reported value for  $^{20}\text{Ne}+^{181}\text{Ta}$  reaction at  $E_{\text{lab}} = 149$  MeV in Ref. [29]. However, the values in the present measurement are much higher than those reported for 60 MeV  $^3\text{He}$  induced reactions on  $^{197}\text{Au}$ ,  $^{203}\text{Tl}$ , and

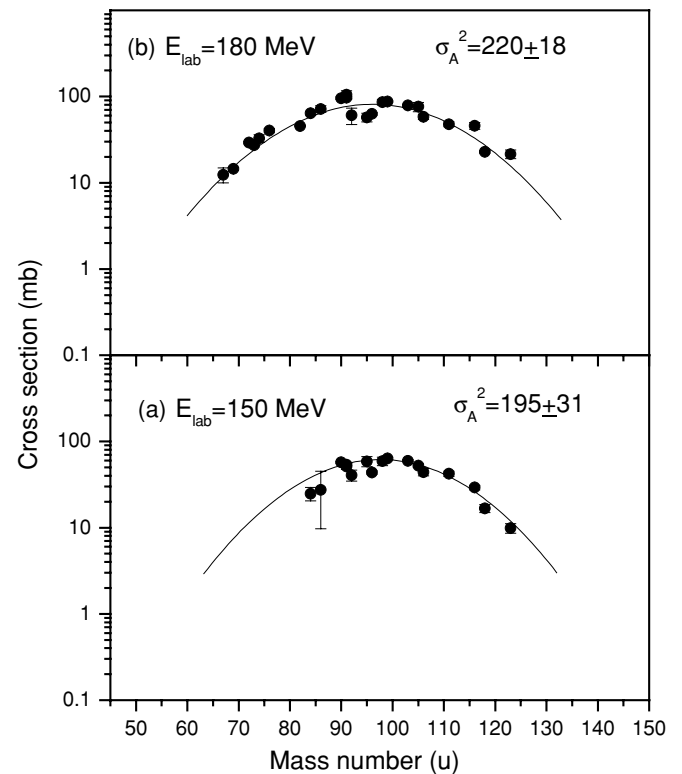


FIG. 2. Mass distribution of the fission products formed in  $^{20}\text{Ne}+^{181}\text{Ta}$  reaction at  $E_{\text{lab}} = 150$  MeV (a) and 180 MeV (b).

$^{205}\text{Tl}$  [30] forming compound nuclei similar to that of the present study. The average angular momentum of the fissioning nucleus ( $l = 46\hbar$  and  $52\hbar$  at  $E_{\text{lab}} = 150$  and  $180$  MeV, respectively) in the present system is much higher compared to that of the fissioning nucleus in  $^3\text{He}$  induced reactions [30] resulting in the higher effective fissility [22] of the compound nucleus. This may result in larger variance of the mass distribution as discussed in Ref. [22]. Fission cross sections obtained by integrating the fitted Gaussian were  $1080 \pm 124$  and  $1509 \pm 140$  mb at  $E_{\text{lab}} = 150$  and  $180$  MeV, respectively. Fission cross sections were also calculated using the statistical model code PACE2 [31]. In the calculations, compound nucleus  $l$ -distribution was generated using the code PACE2 (which uses Bass model [18]) with diffuseness parameter of 0.3. Level density parameter  $a$  was taken as  $A_f/9$   $\text{MeV}^{-1}$ . The ratio  $a_f/a_n$  was taken as unity. The code PACE2 uses finite range fission barrier of Sierk [32] as default value. In the present calculations, fission barrier was increased by 5% to get a reasonably good agreement between the experimental and calculated fission cross sections. The calculated fission cross sections at  $E_{\text{lab}} = 150$  and  $180$  MeV were  $1087$  and  $1320$  mb, respectively. The calculated fission cross section at  $E_{\text{lab}} = 180$  MeV includes about 10% contribution from fast fission arising from the collision trajectories for which there is no fission barrier in the exit channel.

### B. Evaporation residue measurement

Cross section of the evaporation residues formed in  $^{20}\text{Ne}+^{181}\text{Ta}$  reaction at  $E_{\text{lab}} = 150$  and  $180$  MeV are given in Table III. Excitation energy of the compound nucleus in the present study at  $E_{\text{lab}} = 180$  MeV is about  $128$  MeV. Beyec *et al.* [33] have reported the relative yields of the ERs formed in  $^{20}\text{Ne}+^{181}\text{Ta}$  reaction in the compound nucleus excitation energy range of  $60$  to  $140$  MeV. These measurements show

TABLE III. Formation cross section of evaporation residues (ERs) formed in CF and ICF reactions in  $^{20}\text{Ne}+^{181}\text{Ta}$  reaction in at  $E_{\text{lab}} = 150$  and  $180$  MeV.

Nuclide	Cross section (mb)	
	$E_{\text{lab}} = 150$ MeV	$E_{\text{lab}} = 180$ MeV
$^{180}\text{Os}$	–	$13.5 \pm 2.1$
$^{181}\text{Re}$	$18.0 \pm 1.5$	$75.7 \pm 4.5$
$^{182}\text{Re}^g$	$15.6 \pm 0.8$	$46.1 \pm 2.3$
$^{182}\text{Os}$	$5.1 \pm 0.5$	$39.5 \pm 3.5$
$^{183}\text{Re}$	$36.3 \pm 6.0$	$108.0 \pm 8.0$
$^{184}\text{Ir}$	$5.1 \pm 0.4$	$22.2 \pm 1.5$
$^{185}\text{Os}$	$9.6 \pm 0.8$	$24.6 \pm 2.3$
$^{186}\text{Ir}^b$	$2.70 \pm 0.24$	$10.4 \pm 1.4$
$^{188}\text{Pt}$	$5.6 \pm 0.2$	$35.0 \pm 2.0$
$^{189}\text{Pt}$	$8.2 \pm 2.2$	$57.8 \pm 4.6$
$^{190}\text{Hg}$	$13.6 \pm 0.8$	$81.0 \pm 2.3$
$^{191}\text{Hg}^m$	$17.0 \pm 1.4$	$27.6 \pm 4.0$
$^{192}\text{Hg}$	$11.4 \pm 0.7$	$40.1 \pm 1.5$
$^{193}\text{Hg}^m$	$2.02 \pm 0.57$	$1.5 \pm 0.2$
$^{194}\text{Tl}^m$	$3.93 \pm 0.51$	$2.2 \pm 0.2$

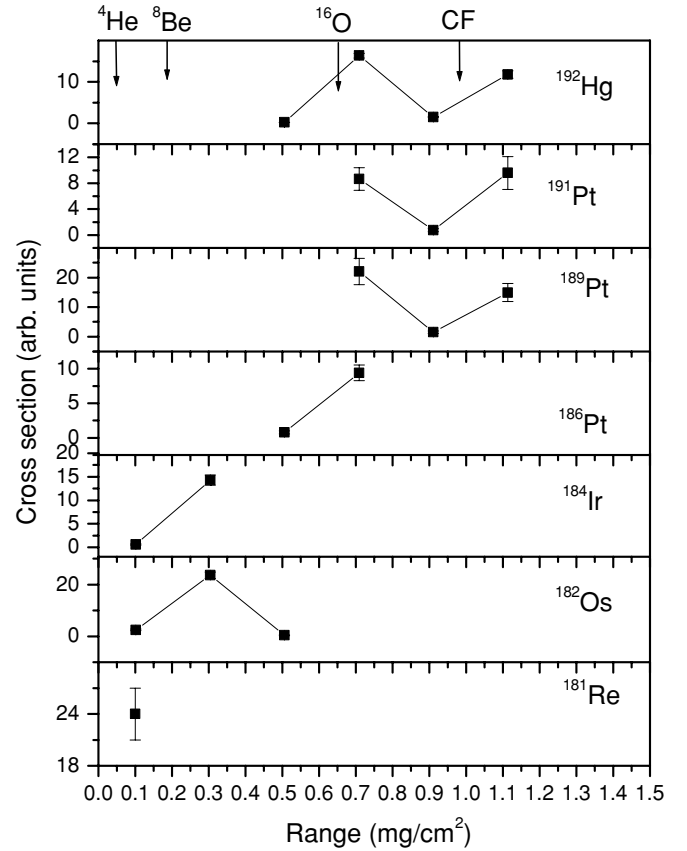
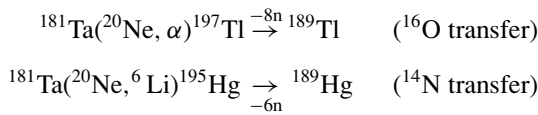


FIG. 3. Recoil range distribution (RRD) of evaporation residues formed in  $^{20}\text{Ne}+^{181}\text{Ta}$  reaction at  $E_{\text{lab}} = 180$  MeV. Arrows mark the calculated ranges corresponding to CF and ICF channels.

that the major ERs formed following complete fusion at  $E_{\text{lab}} = 180$  MeV are  $^{191-193}\text{Bi}$ , which undergo  $\alpha$  and EC decay. Thus, the measured cross section of ERs with mass number greater than 186 may have contribution from both CF and ICF channels. Therefore, measured formation cross sections of ERs with mass number greater than 186 were apportioned into CF and ICF channels using the data of RRDs which could resolve the CF and ICF channels. Figure 3 shows the RRDs of ERs formed in  $^{20}\text{Ne}+^{181}\text{Ta}$  reaction at  $E_{\text{lab}} = 180$  MeV. The different ranges for ERs represent the difference in the linear momentum transfer associated with CF and ICF channels. The recoil range of an ER can be compared with the theoretically calculated values for different ICF channels to obtain the information about the formation channel of the ER. Calculation of the recoil range of an ER requires the knowledge of its recoil energy. The recoil energies of the ERs were calculated using the breakup fusion model [34]. In this model the velocity of the out going particle (ejectile) after ICF is assumed to be the same as that of the projectile. This assumption results in the following expression for the recoil energy  $E_R$  of the nucleus (which gives ER after particle evaporation) formed in ICF reaction:

$$E_R = \frac{M_{\text{tr}}}{M_p} E_{\text{lab}} \frac{M_{\text{tr}}}{M_{\text{tr}} + M_t}, \quad (7)$$

where  $M_{tr}$  is the mass of the nucleons transferred from the projectile to the target nucleus.  $M_p$  and  $M_t$  are the masses of the projectile and the target, respectively. After calculating the recoil energies  $E_R$ , the recoil ranges of ERs were calculated using the code TRIM [35]. In the calculations, the change in  $E_R$  due to the angular distribution of the ejectile has been ignored. Calculated ranges corresponding to different ICF channels, involving transfer of  $^{16}\text{O}$ ,  $^8\text{Be}$ , and  $^4\text{He}$  from the projectile to the target are marked by arrows in Fig. 3. The calculated range corresponding to CF is also marked by an arrow in the figure. The finite thickness of the catcher foils limits the distinction in the linear momentum transfer associated with the ICF channels involving transfer of very similar masses. For example, the difference in the linear momentum transfer in following reactions:



is very small and therefore the RRDs of  $^{189}\text{Tl}$  and  $^{189}\text{Hg}$  is expected to be similar. Further, if the reaction products are short lived as in the present case, their decay products with comparatively longer half-lives are measured. Thus,  $^{189}\text{Pt}$  (measured in the present reaction) may be fed from both  $^{189}\text{Tl}$  and  $^{189}\text{Hg}$ , and the present measurement cannot resolve the ICF channels corresponding to the transfer of  $^{16}\text{O}$  and  $^{14}\text{N}$ . Therefore, a particular transfer channel referred in the discussion includes the transfer of other nuclei with similar masses. RRDs of  $^{192}\text{Hg}$  and  $^{189,191}\text{Pt}$  shows two components. The low range component corresponds to the transfer of  $^{16}\text{O}$  to  $^{181}\text{Ta}$  and the high range component corresponds to complete fusion. RRD of  $^{184}\text{Ir}$  shows that its range corresponds to the transfer of  $^8\text{Be}$ . The range of  $^{182}\text{Os}$  is same as that of  $^{184}\text{Ir}$ , indicating that its precursor is formed in the transfer of  $^8\text{Be}$  to  $^{181}\text{Ta}$ . Range of  $^{181}\text{Re}$  is lowest and corresponds to the  $^4\text{He}$  transfer channel. The data of RRDs of ERs was used to apportion the cross section of ERs having contribution from both CF and ICF channels. It can be seen from Fig. 3 that the ICF products were predominantly stopped in the first four catcher foils and CF products were stopped in the sixth catcher foil. Thus, measured cross section of  $^{192}\text{Hg}$  and  $^{189}\text{Pt}$  were apportioned into CF and ICF channels according to the ratio of their activities in the fourth and sixth catcher foil. Cross section of other ERs (having contribution from both CF and ICF channels) were apportioned using the average value of the ICF contribution obtained from the RRD data of  $^{192}\text{Hg}$  and  $^{189,191}\text{Pt}$ . Since, experimental cross section of an ER may have contribution from more than one ICF channels, it was not possible to ascertain the cross section for individual ICF channels. Therefore, cross sections of ERs were added to get an estimate of the total ICF cross section. The cross section of ERs formed in CF and ICF reactions at  $E_{\text{lab}} = 180$  MeV were determined as  $92 \pm 8$  and  $488 \pm 40$  mb, respectively. At  $E_{\text{lab}} = 180$  MeV, the difference between the calculated fusion [18] and total reaction cross section is 528 mb. Thus, ICF cross section accounts for about almost entire cross section for the noncompound nucleus process above  $l_{\text{crit}}$ .

In the present study, the code HICOL [36,37] was used to simulate the evolution of the collision trajectories resulting in compound and non-compound nucleus processes at  $E_{\text{lab}} = 180$  MeV. In this model the composite system is described by three parameters, namely,  $s$  distance between the centers of the two nuclei,  $\sigma$  neck coordinate, and  $\Delta$  mass asymmetry. The model calculates the change in these parameters with time to give the time dependent development of the collision trajectories. A plot of  $\sigma$  vs  $s$  for  $l = 40\hbar$  and  $85\hbar$  is shown in Fig. 4. The collision trajectory with  $l = 40\hbar$ , is a fusion trajectory which shows a decrease in the distance between the two nuclei approaching each other with the evolution of the neck, finally leading to the formation of the compound nucleus. The collision trajectory with  $l = 85\hbar$  results in noncompound nucleus process. It can be seen from the figure that the distance between the two colliding nuclei first decreases and remains almost constant for some time and then starts increasing until the two fragments separate. Thus, HICOL predicts that the collision trajectories leading to non-compound nucleus process end up in fission like events. However, a reasonable agreement between the experimental and calculated fission cross section suggests that the contribution from such events is not significant. This is consistent with the observation that ICF reaction is the dominant noncompound nucleus process. Also, in the present study, DIC products were not detected indicating that the cross section for DIC is not significant at  $E_{\text{lab}} = 180$  MeV.

At  $E_{\text{lab}} = 150$  MeV,  $l_{\text{max}} (=75\hbar)$  is close to  $l_{\text{crit}} (=69\hbar)$  [18], and contribution from the noncompound nucleus processes is expected to be about 15% of the total reaction cross section. According to Beyec *et al.* [33] the major ERs formed at  $E_{\text{lab}} = 150$  MeV are  $^{192,193}\text{Bi}$ . Therefore, experimentally measured cross sections of ERs with mass number lower than 192 were added to obtain ICF cross section at this beam energy. ICF cross section ( $\sigma_{\text{ICF}}$ ) in  $^{20}\text{Ne}+^{181}\text{Ta}$  reaction at this beam energy is  $139 \pm 17$  mb. As in the case of 180 MeV, DIC products were not detected at this beam energy also. This study indicates that ICF is the dominant noncompound nucleus process in  $^{20}\text{Ne}+^{181}\text{Ta}$  reaction at beam energies of the present study. DIC may be observed in this system at still higher bombarding energies as was observed by Cabrera *et al.* [15] in  $^{20}\text{Ne}+^{169}\text{Tm}$  reaction.

### C. Angular distribution

From the end of irradiation activity ( $A_i$ ) in different strips, the laboratory angular distribution of a given fission product was obtained using the equation

$$W(\theta) = A_i / [\pi \{ \cos(\theta_{1\text{lab}}) - \cos(\theta_{2\text{lab}}) \}], \quad (8)$$

where  $\theta_{1\text{lab}}$  and  $\theta_{2\text{lab}}$  correspond to the two extreme angles for each strip such that the denominator on the right hand side corrects for the solid angle of the strip. The laboratory angular distributions were converted to the center of mass system assuming full momentum transfer to the compound nucleus. Conversion of the laboratory angular distribution to center of mass (c.m.) angular distribution requires the knowledge of the kinetic energy of the fission fragments. Kinetic energies of the fission fragments were calculated

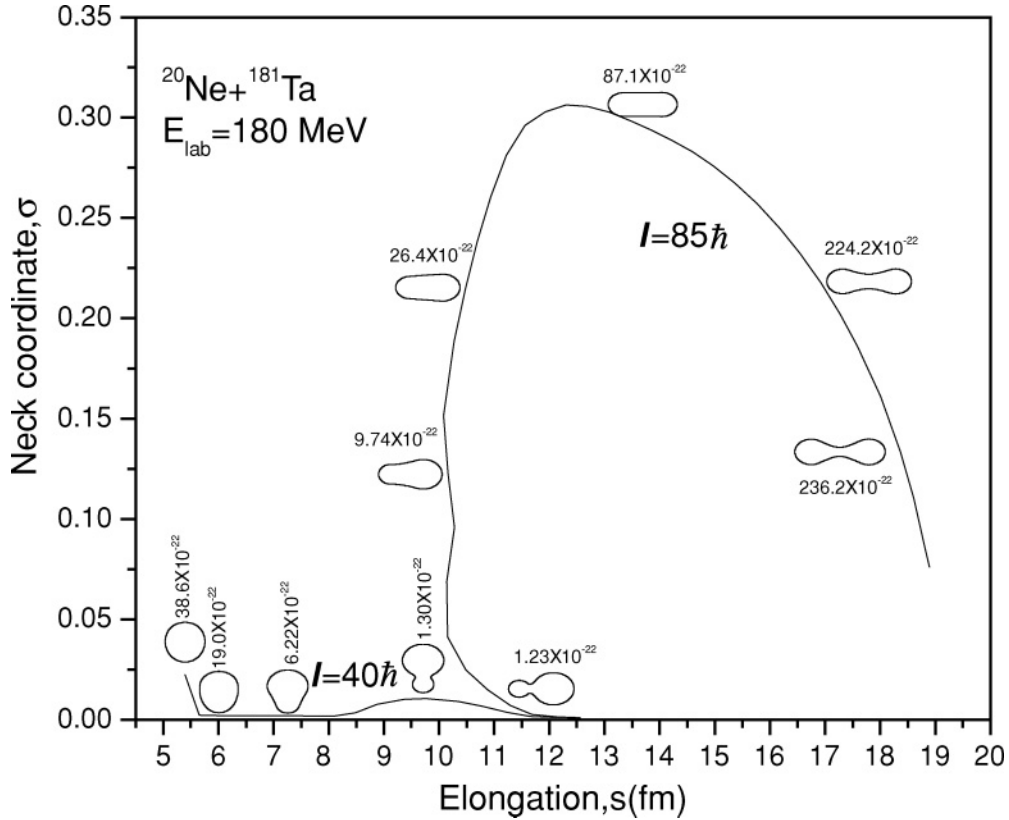


FIG. 4. Collision trajectories for  $l = 40\hbar$  (fusion trajectory) and  $80\hbar$  (trajectory leading to non-compound nucleus process) for  $^{20}\text{Ne}+^{181}\text{Ta}$  reaction at  $E_{\text{lab}} = 180$  MeV. The numbers in the figure represent time-scale of the process in seconds.

using the prescription of Rossner *et al.* [28]. The center of mass angular distribution of fission products were fitted using the statistical theory expression [38]. According to statistical

theory, for a projectile-target system with zero spin, the probability of emission of the fission fragment at an angle  $\theta$  with respect to beam direction, is given by

$$W(\theta) \propto C \sum_{l=0}^{\infty} \frac{(2l+1)^2 T_l \exp[-(l+1/2)^2 \sin^2 \theta / 4K_0^2] J_0 [i(l+1/2)^2 \sin^2 \theta / 4K_0^2]}{(2K_0^2)^{1/2} \text{erf}[(l+1/2)/(2K_0^2)^{1/2}]}, \quad (9)$$

where  $T_l$  is the transmission coefficient for the  $l^{\text{th}}$  partial wave.  $K_0^2$  is the variance of the  $K$  distribution,  $K$  being the projection of the angular momentum vector on the symmetry axis of the fissioning nucleus.  $J_0$  is the zeroth order Bessel function. The constant  $C$  has been introduced in Eq. (9) to normalize the calculated angular distribution to the experimental angular distribution. The experimental angular distributions were fitted using equation (9) with  $C$  and  $K_0^2$  as free parameters. The  $l$  distribution of the compound nucleus was calculated using the code PACE2 [31]. The experimental and fitted angular distributions were normalized with respect to the fitted value of  $W(90)$ . The angular distributions at  $E_{\text{lab}} = 150$  and  $180$  MeV along with the fitted curves are shown in Figs. 5 and 6, respectively. The experimental anisotropies ( $W(0)/W(90)$ )

of the angular distributions of various fission products were determined from the fitted curves. Plots of experimental anisotropy vs mass asymmetry ( $A_H/A_L$ ) at  $E_{\text{lab}} = 150$  and  $180$  MeV are shown in Figs. 7(a) and 7(b), respectively,  $A_H$  and  $A_L$  are the mass numbers of the heavy and light fission products, respectively, for a particular mass split. It can be seen from the figures that the angular anisotropy is not correlated with the mass asymmetry in the present system as was observed in the proton and alpha particle induced fission [19–21]. The fission product angular distributions were fitted together using Eq. (9) to obtain average anisotropy at the two energies. The average anisotropies determined at  $E_{\text{lab}} = 150$  and  $180$  MeV were  $4.29 \pm 0.12$  and  $4.21 \pm 0.12$ , respectively. The solid lines in the Figs. 7(a) and 7(b), represent average anisotropies.

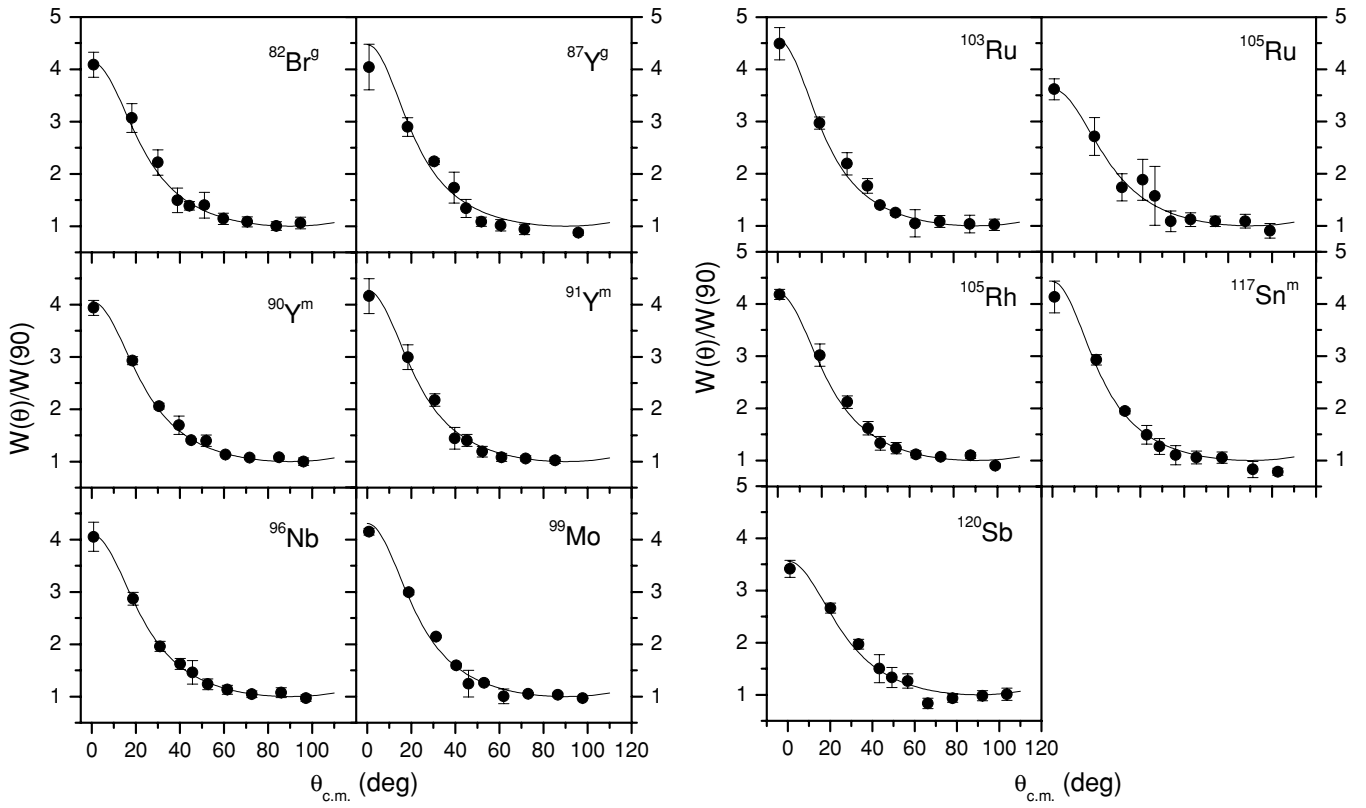


FIG. 5. Centre of mass angular distribution of fission products formed in  $^{20}\text{Ne}+^{181}\text{Ta}$  reaction at  $E_{\text{lab}} = 150$  MeV.

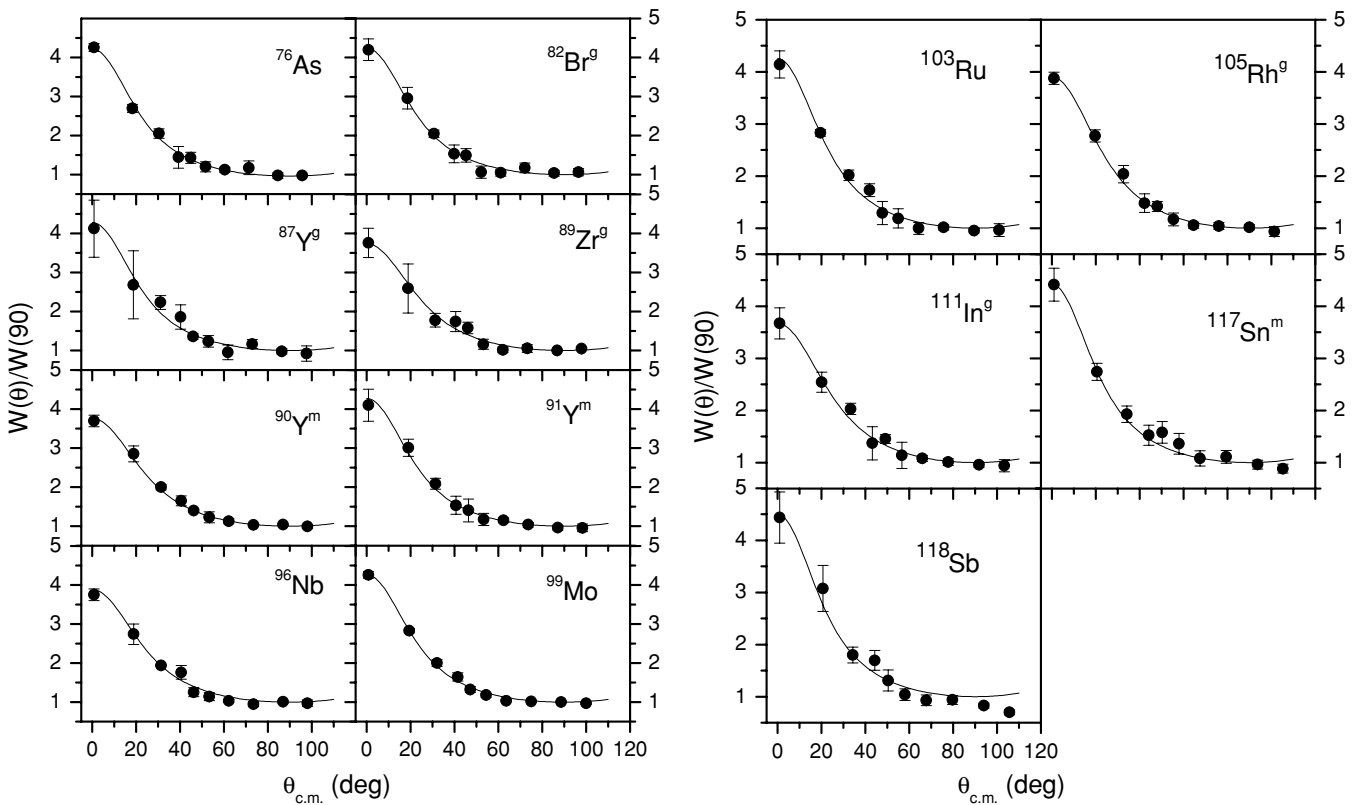


FIG. 6. Centre of mass angular distribution of fission products formed in  $^{20}\text{Ne}+^{181}\text{Ta}$  reaction at  $E_{\text{lab}} = 180$  MeV.

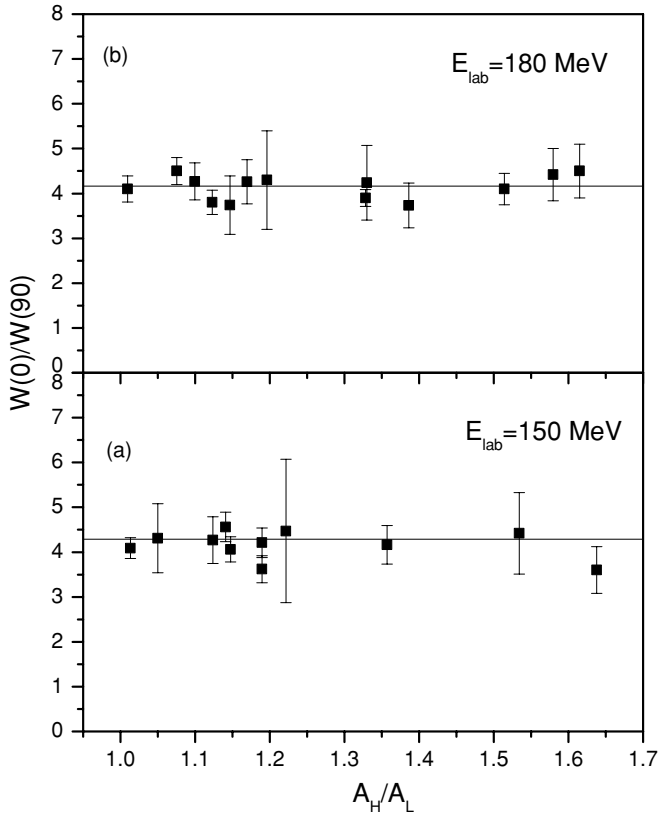


FIG. 7. Plot of angular anisotropy vs mass asymmetry of fission products formed in  $^{20}\text{Ne}+^{181}\text{Ta}$  reaction at  $E_{\text{lab}} = 150$  MeV (a) and 180 MeV (b).

At higher excitation energies and angular momentum of the compound nucleus, many deviations from the statistical theory have been reported [39–42]. In order to test the applicability of the statistical theory to the present system, angular anisotropies were calculated using Eq. (9). The calculation of angular anisotropy using Eq. (9) requires the knowledge of the transmission coefficient  $T_l$  for different  $l$ -waves leading to fission and the variance of  $K$ -distribution  $K_0^2$ . In view of the large excitation energy of the compound nucleus in the present system, the fusion  $l$ -distribution as calculated using the code PACE2 was taken as the  $l$ -distribution of the fissioning nucleus.  $K_0^2$  is given by the following equation:

$$K_0^2 = I_{\text{eff}} T / \hbar^2, \quad (10)$$

$I_{\text{eff}}$  is the effective moment of inertia of the fissioning nucleus as given by

$$I_{\text{eff}}^{-1} = I_{\parallel}^{-1} - I_{\perp}^{-1}, \quad (11)$$

where  $I_{\parallel}$  and  $I_{\perp}$  are the moments of inertia for the rotation about the symmetry axis, and about the axis perpendicular to the symmetry axis, respectively.  $T$  is the temperature of the fissioning nucleus at the saddle point. The temperature  $T$  of the fissioning nucleus was calculated using the following expression:

$$T = \sqrt{(E^* - B_f - E_{\text{rot}} - E_v) / (A_f / 9)}, \quad (12)$$

TABLE IV. Experimental and calculated anisotropies of angular distribution of fission products for  $^{20}\text{Ne}+^{181}\text{Ta}$  reaction at  $E_{\text{lab}} = 150$  and 180 MeV.

$E_{\text{lab}}$ (MeV)	Angular anisotropy ( $W(0)/W(90)$ )			
	Experimental		Calculated	
150	$4.29 \pm 0.13$	4.76 <sup>a</sup>	4.60 <sup>b</sup>	4.45 <sup>c</sup>
180	$4.21 \pm 0.12$	4.80 <sup>a</sup>	4.34 <sup>b</sup>	4.24 <sup>c</sup>

<sup>a</sup>Calculated with constant value of  $K_0^2$  corresponding to  $\langle l \rangle$  of the fissioning nucleus.

<sup>b</sup>Calculated with  $l$ -dependent  $K_0^2(l)$ .

<sup>c</sup>Calculated with  $l$ -dependent  $K_0^2(l)$ , after correcting for the angular momentum removed by prefission neutrons.

where  $E^*$  is the excitation energy of the compound nucleus,  $B_f$  is the fission barrier,  $E_{\text{rot}}$  is the rotational energy,  $E_v$  is the energy lost in the emission of prefission neutrons and  $A_f$  is the mass of the fissioning nucleus.  $E_{\text{rot}}$  was approximated as  $l^2 \hbar^2 / 2I_{\perp}$ . The  $\nu_{\text{pre}}$  values were calculated as 3.6 and 5.0 at  $E_{\text{lab}} = 150$  and 180 MeV, respectively [26] and were used for the calculation of  $E_v$ .  $I_{\text{eff}}$ ,  $B_f$ , and  $E_{\text{rot}}$  were calculated using the rotating finite range model (RFRM) of Sierk [32]. In the RFRM calculations, mass of the fissioning nucleus was taken as 197 and 196 at  $E_{\text{lab}} = 150$  and 180 MeV, respectively. The  $K_0^2$  values at both the energies were calculated using the  $I_{\text{eff}}$  value corresponding to the average angular momentum  $\langle l \rangle$  of the fissioning nucleus. Angular anisotropies calculated using the constant values of  $K_0^2$  were found to be higher (Table IV) than the experimental anisotropies. Fission trajectories with high  $l$ -values are expected to have very small or no fission barrier. Therefore, equilibrium deformation for high  $l$ -trajectories will be nearly spherical, resulting in the sharp rise of  $I_{\text{eff}}$  and in turn, of  $K_0^2$  at higher  $l$ -values. Thus, at these bombarding energies, constant value of  $K_0^2$  cannot reproduce the experimental anisotropies. The angular anisotropies calculated using the  $l$ -dependent  $K_0^2$  values in Eq. (9) are close to the experimental anisotropies. However, the calculated values are on the higher side at both the energies. PACE2 calculations show that the average spin removed by one prefission neutron is  $0.5\hbar$  and  $0.6\hbar$  at  $E_{\text{lab}} = 150$  and 180 MeV, respectively. Therefore, angular momentum of the fissioning nucleus was reduced by  $2\hbar$  and  $3\hbar$  at  $E_{\text{lab}} = 150$  and 180 MeV, respectively, to account for the angular momentum removed by the prefission neutrons. It can be seen in the Table IV that the angular anisotropies calculated after considering the angular momentum removed by the pre-fission neutrons are in good agreement with the experimental values.

For the present system, several  $l$ -waves below  $l_{\text{crit}}$  are also expected to contribute to noncompound nucleus fission. With increasing  $l$ , the elongation of the pocket configuration [9] in the entrance channel increases and the saddle point elongation of the fissioning nucleus decreases. Thus, beyond certain  $l$ -value, pocket configuration becomes more elongated than the saddle point and the collision trajectories may not be trapped inside the saddle point and would, therefore, result in noncompound nucleus fission [9]. For the collision between  $^{20}\text{Ne}$  and  $^{181}\text{Ta}$ , entrance channel potential was calculated

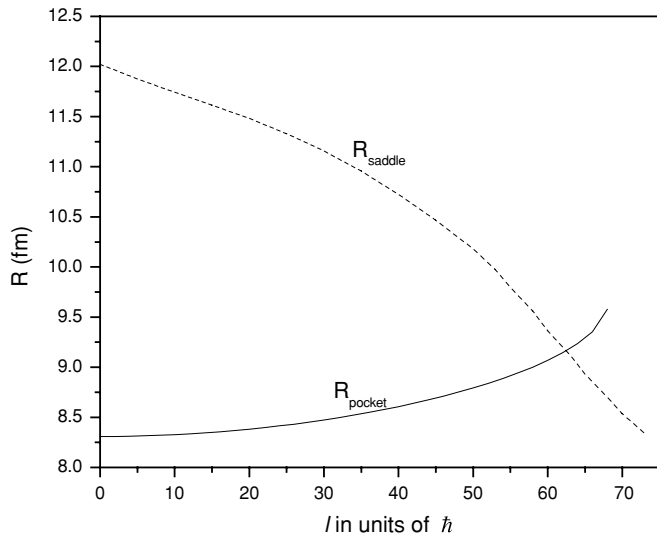


FIG. 8. Plot of elongation of the pocket configuration ( $R_{\text{pocket}}$ ) for the collision trajectories for  $^{20}\text{Ne}+^{181}\text{Ta}$  reaction (Solid line) and saddle point elongation ( $R_{\text{saddle}}$ ) of  $^{201}\text{Bi}$  (dashed line) as a function of angular momentum.

using the formalism given in Ref. [43] and elongation of the pocket configuration for the collision trajectories with different  $l$ -values was determined. Plot of the elongation of the pocket configuration as a function of  $l$ -value is shown in Fig. 8 as solid line. The increase in angular momentum increases the fissility of the compound nucleus. Both angular momentum and fissility of the compound nucleus are related to the fission barrier. A plot of fissility vs RFRM fission barrier [32] was fitted to a third order polynomial and the coefficients of the fitted curve were used to translate the effect of the angular momentum on compound nucleus  $^{201}\text{Bi}$  into a change in the fissility. In order to locate the saddle point corresponding to different  $l$ -values (fissilities), deformation energy of  $^{201}\text{Bi}$  was calculated using the procedure of Brack *et al.* [44]. The saddle point elongation of  $^{201}\text{Bi}$  for different  $l$ -values is shown in the Fig. 8 as dashed line. It is seen from the figure that the collision trajectories with  $l < 63\hbar$  have pocket configuration less elongated compared to the corresponding saddle point elongation and, therefore, such trajectories are expected to result in compound nucleus formation. For the collision trajectories with  $l > 63\hbar$ , pocket configuration is more elongated compared to the corresponding saddle point configuration and such trajectories are expected to result in noncompound nucleus fission [9]. Based on this picture, the contribution for noncompound nucleus fission is expected to be 19% and 35% of the total fission cross section at  $E_{\text{lab}} = 150$

and 180 MeV, respectively. In the case of noncompound nucleus fission, the composite nucleus formed after fusion of the projectile and the target, is not captured inside the saddle point and undergoes fission without formation of a fully equilibrated compound nucleus. In such a situation, the composite nucleus retains a memory of the entrance channel  $K$ -distribution resulting in an angular anisotropy value which is different from statistical theory calculation [10]. However, no significant deviation from the statistical theory calculation was observed in the present measurement. This may be due to the fact that during the motion of the composite system towards adiabatic potential, the relaxation in the radial degree of freedom may bring the composite system inside the saddle point. In this case, fission will occur from fully equilibrated compound nucleus and the experimental angular distribution is expected to be consistent with the statistical theory calculation. Another possibility is that the fissioning nucleus equilibrates in its all degrees of freedom at the turning point of its trajectory.

#### IV. CONCLUSIONS

Mass and mass resolved angular distribution of the fission products and recoil range distribution of the evaporation residues have been measured to obtain information about the different reaction channels in the  $^{20}\text{Ne}+^{181}\text{Ta}$  reaction at  $E_{\text{lab}} = 150$  and 180 MeV. The variances of the mass distributions have been found to compare well with the value reported in literature for the similar system with comparable excitation energy and angular momentum. However, the variances of the mass distributions in the present study have been found to be higher than those for the systems involving lower angular momentum. Incomplete fusion reaction has been observed as the dominant non-compound nucleus process. DIC products could not be detected indicating that contribution from DIC reactions is not significant in the  $^{20}\text{Ne}+^{181}\text{Ta}$  reaction in the energy range of the present study. Measurement of the mass resolved angular distribution of the fission products has shown that the angular anisotropy is not correlated with the mass asymmetry in the present system. Angular distribution of the fission products were fitted together to obtain average anisotropy. Though significant contribution from non-compound nucleus fission is expected, based on the comparison of the elongation of the pocket configuration with the saddle point elongation, experimental anisotropies could be reasonably reproduced by the statistical theory calculation after using the angular momentum dependent  $K_0^2(l)$  and considering the removal of the angular momentum by the pre-fission neutrons.

- [1] J. Blocki, J. Randrup, W. J. Swiatecki, and C. F. Tsang, *Ann. Phys. (NY)* **105**, 427 (1977).  
 [2] J. Töke *et al.*, *Nucl. Phys.* **A440**, 327 (1985).  
 [3] A. Gobbi and W. Nörenberg, in *Heavy Ion Collisions*, edited by R. Bock (North-Holland, Amsterdam, 1980), Vol. 2.  
 [4] K. Siwek-Wilczynska, E. H. du Marchie van Voorthuysen, J. van Popta, R. H. Siemssen, and J. Wilczynski, *Phys. Rev. Lett.* **42**, 1599 (1979).

- [5] T. Inamura, M. Ishihara, T. Fakuda, T. Shimoda, and H. Hiruta, *Phys. Lett.* **B68**, 51 (1977).  
 [6] B. S. Tomar, A. Goswami, G. K. Gubbi, A. V. R. Reddy, S. B. Manohar, B. John, and S. K. Kataria, *Phys. Rev. C* **58**, 3478 (1998).  
 [7] K. Surendra Babu, R. Tripathi, K. Sudarshan, S. Sodaye, A. Goswami, B. D. Shrivastava, and B. S. Tomar, *Nucl. Phys.* **A739**, 229 (2004).

- [8] W. J. Swiatecki, Phys. Scr. **24**, 113 (1981).
- [9] C. Gregoire, C. Ngo, and B. Remaud, Phys. Lett. **B99**, 17 (1981); Nucl. Phys. **A383**, 392 (1982).
- [10] V. S. Ramamurthy and S. S. Kapoor, Phys. Rev. Lett. **54**, 178 (1985).
- [11] D. J. Hinde, M. Dasgupta, J. R. Leigh, J. P. Lestone, J. C. Mein, C. R. Morton, J. O. Newton, and H. Timmers, Phys. Rev. Lett. **74**, 1295 (1995).
- [12] A. C. Berriman, D. J. Hinde, M. Dasgupta, C. R. Morton, R. D. Butt, and J. O. Newton, Nature **413**, 144 (2001).
- [13] R. N. Sagaidak *et al.*, Phys. Rev. C **68**, 014603 (2003).
- [14] J. G. Keller, B. B. Back, B. G. Glagola, D. Henderson, S. B. Kaufman, S. J. Sanders, R. H. Siemssen, F. Videbaek, B. D. Wilkins, and A. Worsham, Phys. Rev. C **36**, 1364 (1987).
- [15] J. Cabrera *et al.*, Phys. Rev. C **68**, 034613 (2003).
- [16] G. J. Mathews, J. B. Moulton, G. J. Wozniak, B. Cauvin, R. P. Schmitt, J. S. Sventek, and L. G. Moretto, Phys. Rev. C **25**, 300 (1982).
- [17] H. Ikezoe *et al.*, Z. Phys. A **330**, 289 (1988).
- [18] R. Bass, Phys. Lett. **B47**, 139 (1973).
- [19] A. Goswami, S. B. Manohar, S. K. Das, A. V. R. Reddy, B. S. Tomar, and S. Prakash, Z. Phys. A **342**, 299 (1992).
- [20] T. Datta, S. P. Dange, H. Naik, and S. B. Manohar, Phys. Rev. C **48**, 221 (1993).
- [21] N. Takahashi, N. Ykawa, H. Kobayashi, A. Yokoyama, T. Saito, and H. Baba, Z. Phys. A **353**, 35 (1995).
- [22] R. Tripathi, K. Sudarshan, A. Goswami, P. K. Pujari, B. S. Tomar, and S. B. Manohar, Phys. Rev. C **69**, 024613 (2004).
- [23] U. Reus and W. Westmeier, At. Data Nucl. Data Tables **29**, 1 (1983).
- [24] Table of Isotopes, 8th edition, Vol. I&II, Richard B. Firestone, V. S. Shirley Ed., John Wiley and Sons, Inc.
- [25] H. Freiesleben and J. V. Kratz, Phys. Rep. **106**, 1 (1984).
- [26] E. M. Kozuline, A. Ya. Rusanov, and G. N. Smirenkin, Phys. At. Nucl. **56**, 166 (1993).
- [27] W. J. Swiatecki, J. Phys. (Paris) **33**, C5-45 (1972).
- [28] H. H. Rossner, J. R. Huizenga, and W. U. Schroder, Phys. Rev. Lett. **53**, 38 (1984).
- [29] D. J. Hinde, H. Ogata, M. Tanaka, T. Shimoda, N. Takahashi, A. Shinohara, S. Wakamatsu, K. Katori, and H. Okamura, Phys. Rev. C **39**, 2268 (1989).
- [30] E. N. Gruzintsev, M. G. Itkis, V. N. Okolovich, and V. N. Smirenkin, Yad. Fiz. **39**, 1336 (1984).
- [31] A. Gavron, Phys. Rev. C **21**, 230 (1980).
- [32] Arnold J. Sierk, Phys. Rev. C **33**, 2039 (1986).
- [33] Y. Le Beyec, M. Lefort, J. Livet, N. T. Porile, and A. Siivola, Phys. Rev. C **9**, 1091 (1974).
- [34] T. Udagawa and T. Tamura, Phys. Rev. Lett. **45**, 1311 (1980).
- [35] J. P. Biersack and J. F. Ziegler, TRIM 95.06, 1995.
- [36] H. Feldmeier, Rep. Prog. Phys. **50**, 915 (1987).
- [37] H. Feldmeier and H. Spangenberg, Nucl. Phys. **A435**, 229 (1985).
- [38] R. Vandenbosch and J. R. Huizenga, *Nuclear Fission* (Academic, New York, 1973).
- [39] C. R. Morton, D. J. Hinde, A. C. Berriman, R. D. Butt, M. Dasgupta, A. Godley, and J. O. Newton, Phys. Lett. **B481**, 160 (2000).
- [40] D. J. Hinde, A. C. Berriman, M. Dasgupta, J. R. Leigh, J. C. Mein, C. R. Morton, and J. O. Newton, Phys. Rev. C **60**, 054602 (1999).
- [41] C. R. Morton, A. C. Berriman, R. D. Butt, M. Dasgupta, A. Godley, D. J. Hinde, and J. O. Newton, Phys. Rev. C **62**, 024607 (2000).
- [42] H. Rossner, D. Hilscher, E. Holub, G. Ingold, U. Jahnke, H. Orf, J. R. Huizenga, J. R. Birkelund, W. U. Schröder, and W. W. Wilcke, Phys. Rev. C **27**, 2666 (1983).
- [43] H. Ngo and C. Ngo, Nucl. Phys. **A348**, 140 (1980).
- [44] M. Brack, Jens Damgaard, A. S. Jensen, H. C. Pauli, V. M. Strutinsky, and C. Y. Wong, Rev. Mod. Phys. **44**, 320 (1972).